Video Article

Plasma Actuators in Rarefied Super/Hypersonic Flows: Experimental Work to Enhance Spacecraft Control and Deceleration During Atmospheric Entries

Sandra Coumar[1], Viviana Lago[1]

[1]ICARE, CNRS, UPR 3021

Correspondence to: Sandra Coumar at sandra.coumar@cnrs-orleans.fr

URL: https://www.jove.com/video/56602
DOI: doi:10.3791/56602

Keywords: Gas and plasma physics, compressible aerodynamics, super/hypersonic flows, atmospheric entries, aerospace engineering, rarefied flows, wind tunnel, shock wave, spacecraft control

Date Published: 7/31/2017

Citation: Coumar, S., Lago, V. Plasma Actuators in Rarefied Super/Hypersonic Flows: Experimental Work to Enhance Spacecraft Control and Deceleration During Atmospheric Entries. *J. Vis. Exp.* (), e56602, doi:10.3791/56602 (2017).

Abstract

During an atmospheric reentry mission, deceleration is a major issue. The main way to slow down a vehicle is to rely on the drag force induced by the friction with the air. However, due to the high speeds reached by the vehicle, the friction induces intense heating of the structure of the vehicle. To counter this, the authors present a new method based on the ionization of the flow around the vehicle with a plasma actuator leading to the deceleration of the vehicle. The main point of this technique is that it allows the vehicle to be slowed in the highest layers of the atmosphere before it endures the harsh conditions produced by atmospheric friction.

This paper introduces the implementation of the plasma actuator on a beveled flat plate, which is a classic model in aerodynamic studies. The reentry conditions are simulated with the super/hypersonic low-density wind tunnel MARHy (Mach Adaptable Rarefied Hypersonic) located in the ICARE laboratory. The method involves two steps: the manufacturing of the plasma actuator and the settling of the wind tunnel to deliver the chosen flow conditions. The experimental setup is carefully designed for high-speed flows, high temperatures and, in our case, low pressures.

For the study of aerodynamics, three types of diagnostics are utilized: an intensified camera for the visualization of the flow, an infrared camera to follow the evolution in time of the distribution of the surface temperatures, and a Pitot probe used for the mapping of the flow pressures around the model. This method is used as the basis for our experiments and is adapted according to the flow later generated by the wind tunnel, the shape of the plasma actuator, or the applied diagnostics.

Introduction

Every space or ballistic mission consists of three phases: launch, flight, and reentry[1]. A successful mission depends on adequate management of the three phases, yet atmospheric reentry has continued to pose major challenges over the past several decades. The very high speeds reached by the vehicle during reentries induce extreme conditions and at least three reentry tasks should be approached with care: deceleration, heating management, and accuracy of the vehicle localization and velocity when landing. Aerodynamic forces, such as drag and lift, become increasingly important as the altitude decreases and usually become dominant at 40 km. This is due to the exponential increase of the air density as distance to the ground decreases. At such altitudes, the drag force plays a key role over all others, including gravity and lift. It influences deceleration and thereby, the heat loads, vehicle design, and re-entry trajectory. Controlling the drag force is a method of directly influencing the deceleration and, therefore, the re-entry conditions.

Previous work carried out by our team showed that plasma actuators induce an increase in the drag force[2] on the model surface and thus, reduce the local heat flux. This effect is obtained by the modification of the shock wave shape that arises when the plasma actuator is on. Therefore, plasma actuators can be classified as a flow control method and compared to traditional techniques. The key strengths of plasma actuators are their low weight and size and relatively low energy consumption. These assets make them promising for flight control systems at high velocities[3]. Hypersonic missions are of great interest, though most of the technologies for hypersonic flow control are complex, time-, and energy-consuming, whereas plasma actuators could be a smart alternative.

However, although many studies deal with plasma control applied to supersonic flows[4,5,6,7,8,9,10], few concern rarefied flows, and still fewer focus on experimental analyses. The most striking project in the field of plasmas for aerodynamic purposes is the Ajax project. This project has the merit of highlighting the possibilities of the use of plasmas to influence aerodynamics, but as this was focused on Aeronautics and not space sciences, attempts focused on drag reduction. In 1968, Cahn *et al.*[11] in the United States also reported experiments conducted on electrostatic-influenced flows. Therefore, work on this subject has been conducted for many years, though mostly working at pressures higher than that in our experimental conditions, as indicated by the use of the Schlieren technique. Since the mid-1990s, publications in the field of plasma control have exploded. Roth[12] shows that the number of "plasma actuator" entries in an online search has been increasing exponentially since 2003. But, the role of the Electro Hydrodynamic (EHD) effect is much less clear in the case of supersonic flow conditions[13,14] and thermal effects are often forward. Other works are available but they are essentially only numerical analyses[15,16]. Therefore, they are complementary to experimental work but cannot be a substitute, especially for validating a theoretical hypothesis.

The specific aim of our team is to make use of the wind tunnel MARHy located in the ICARE laboratory to simulate super/hypersonic low-pressure flows, representing different altitudes, to study the implementation of plasma actuators designed to influence the drag on a vehicle during reentry. Hence, the present work provides complementary databases and knowledge to other researchers working at higher pressure and thus, a higher Reynolds number. Our work is unique because we focus on high altitude supersonic and hypersonic applications, which means lower pressures than the studies from other teams. Moreover, we try to increase the drag force for easier control of the spacecraft, whereas the typical approach is to try to decrease it and control the boundary layer separation. Thus, we believe that our research is innovative and complementary to that conducted by other authors in the super/hypersonic domain. Moreover, we have experimental facilities, which allow us to carry out experimental research in the rarefied supersonic/hypersonic domain that can simulate altitudes between 60 and 140 km with Mach numbers ranging between 2 and 20. These experimental results can be useful for the numerical analysis community, which simulates the effects of plasma actuators under such conditions and might need experimental results for the validation of theoretical findings.

Protocol

1. Experimental Planning

1. Follow instructions and safety precautions before entering the wind tunnel's hall. Safety training can be required for new users.
2. Schedule the experiments in advance and consider the details of the experiments. After selecting the model to be studied, characterize the plasma actuator: its size, shape, and position on the model.
3. Think about the goal of the study and the expected results to install and prepare the diagnostic tools.
4. Organize the wind tunnel supplies, such as the order of gas bottles, if needed.

2. Preparation of the Research Object

1. **Manufacturing the plasma actuator**
    1. Manufacture a stencil in the shape and dimensions of the active electrode and, if needed, another one for the grounded electrode. In this paper, both electrodes are rectangular but with rounded corners, with a radius of curvature of 6 mm, in order to avoid electrostatic edge effects. The length of each electrode is 50 mm with a width of 35 mm representing a covering of 35% of the model surface (see **Figure 1**).
    2. Cut the electrodes using the stencil in the aluminum adhesive. This adhesive is selected as the electrode material because of its small thickness (a few micrometers), high temperature resistance, and high electrical conductivity, all of which minimize losses.
    3. Gently remove the adhesive paste with acetone without creasing the electrode.

2. **Preparation of the flat plate**
    1. Design the model taking into account the size of the flow core. In this study, the model is a beveled flat plate of 100 mm-length, 50 mm-width, 4 mm-thickness and 15° leading edge angle. Choose an electrically insulating and heat-resistant material, because ionizing the gas can deform the model. Here, the model is made of quartz (see **Figure 1**).
    2. Drill a hole of 2 mm diameter at 0.7 mm from the left side of the flat plate and 12 mm from its leading edge. For this purpose, use a diamond hollow drill of 2 mm diameter. The hole (Hole 1) is used as a passage for the screw that will hold the high-voltage cable and the model together (see **Figure 2**). The position of the hole is estimated to be minimally cumbersome and placed on the surface of the active electrode.
    3. Drill another hole of 2 mm diameter at 0.7 mm from the left side of the flat plate, but this time 70 mm from the leading edge. This hole (Hole 2) is the passage for the screw that will maintain the grounded cable and the model together (see **Figure 2**).
    4. Scrape the surface on which the plasma actuator is to be placed with 240 grade sandpaper. This will help create roughness and improve the electrode laying.
    5. With great care, clean the model with a 60% rubbing alcohol and make sure there are no particles left on the surface.

3. **Implementation of the plasma actuator on the model.**
    1. Spread a thin even layer of RTV (Room Temperature Vulcanizing) glue with a brush on the back of the electrodes and remove the excess glue to avoid adding thickness between the plate and the electrode. The chosen glue should endure high-temperatures, going to at least 600 °C. Moreover, choose glue with a dilatation coefficient between those of quartz and aluminum to reduce tension.
    2. Place the active electrode close to the leading edge and press it firmly to expel air bubbles. Indeed, if air bubbles remain, they will inflate when the static pressure decreases and this will lead to detachment of the electrode.
    3. Follow the same procedure as in 2.3.1 and 2.3.2 for the grounded electrode and apply it at a distance of 2.5 cm from the active electrode.
    4. Flip the flat plate over and add something heavy on top of it. This will flatten the electrodes against the flat plate.
    5. Let the whole setup dry for 24 h; the glue should be totally dry. Follow the instructions of the glue; some require heating in an oven.
    6. Use black paint which can withstand high temperatures to draw a line along the central axis of the flat plate and two perpendicular lines passing through the center of each electrode (see **Figure 3**). These lines ensure a good emissivity for the infra-red thermography as the emissivity of the electrodes is low ($\varepsilon < 0.1$ for bare aluminum foil).

3. Installation of the Setup in the Wind Tunnel

1. **Installation of the setup on the standing pole**
    1. Set the standing pole in the test chamber of the wind tunnel, taking into consideration the distance over which the flow would remain uniform (see **Figure 4** and **Figure 5**).

2. Fix the model on the standing pole. It is essential that the whole setup is electrically insulated to avoid electrical interaction with the discharge.
3. Set the appropriate angle of attack, defined as the angle between the flow axis and the model reference length (longitudinal model axis), with an angle gauge. Here, the angle of attack is 0°. Therefore, the trailing edge of the model would always coincide with the flow axis. Check that the model remains in the core of the flow (see **Figure 6**).
4. Set a 1 mm wire-diameter K-type thermocouple to get the static temperature. Place it in the test chamber opposite the model, at least 30 cm from the model in order to avoid interactions with the flow.

2. **Wiring of the plasma actuator**
    1. Screw the high-voltage cable to the active electrode through Hole 1.
    2. Put some insulating glue on the top and end of the screw to avoid arcing when firing the electrode.
    3. Tape the cable to the standing pole with Kapton adhesive to prevent it from moving and disturbing the flow. If necessary, insulate exposed conductive material with the Kapton adhesive.
    4. Connect the generator to the high-voltage cable through the vacuum-tight connection. The generator should deliver -10 kV and 100 mA.
    5. Repeat steps 3.2.1 to 3.2.3 with the ground cable but fix it through Hole 2.
    6. With a multimeter, check the electrical insulation between the cathode and the anode and between the cathode and the test chamber.

4. Setting the Diagnostic Tools

1. **Installation of the Pitot probe**
    1. Manufacture the Pitot probe, keeping in mind that it must not interact with the discharge (so, preferably use glass as the material), with a diameter small enough to avoid flow obstruction but not too small to allow reasonable acquisition times[17,18,19].
    2. Place the Pitot tube in the arm of the 3-axis displacement robot (RTA system). The robot is managed via a motion controller, in this case the National Instruments PXI-7344 (see **Figure 7**).
    3. Connect the Pitot tube to the manometer via a plastic tube and seal the connection with a heat shrink.
    4. Set a bypass for the Pitot tube exit to empty the Pitot tube before each new measurement during the test. This will help to initialize the results.
    5. Position the Pitot on the leading edge of the flat plate with the displacement robot. This sets the starting coordinates (X=0 cm, Y=0 cm, Z=0 cm).
    6. Initialize the LabVIEW program meant for data acquisitions for this new test session.

2. **Installation of the iCCD (Intensified Charge-Coupled Device) camera**
    1. Position the camera on the holder and target the setup through the fluorine window (see **Figure 8**). The camera must capture the full side view of the whole flat plate and especially the upper part of the model. Check that the iCCD camera is aligned horizontally with the flat plate axis.
    2. Improve the sharpness of the image communicated by the camera by focusing on one edge of the flat plate.
    3. Take a set of images of the flat plate. They will help for further data comparisons as they show the experimental setup with no disturbances.

3. **Installation of the IR (Infra-Red) camera**
    1. Position the camera on the holder and target the setup through the zinc selenide window (see **Figure 8**). The camera must center the whole flat plate.
    2. Improve the sharpness of the image communicated by the camera by focusing on the upper surface of the flat plate where lines were painted in black, as defined in 2.3.6.
    3. Measure the surface temperature simultaneously with both the IR camera and a K-type thermocouple flush mounted on the flat plate surface. The temperature measured by the IR camera may differ from the one measured by the thermocouple, as the initial calibration of the camera sets the emissivity ε at 1. If so, estimate the real emissivity of the black paint as the ratio of the temperature given by the thermocouple to the temperature given by the IR camera.
    4. Apply the real emissivity to the IR camera calibration to obtain the real surface temperatures with this device.
    5. Set an adequate camera sensitivity range according to the expected results during the test.

5. Running the Facility

1. Check the toric joint of the door of the test chamber before closing it and tighten at least one of the two wing nuts to press the door.
2. Close all the openings of the wind tunnel.
3. Check that the oil of the vane pumps is above the minimum level. If not, fill the reservoir.
4. Choose the pumping mode according to the needed static (8 Pa) and stagnation (1,214 Pa) pressures. Some pumping configurations are scheduled in two steps. If this is the case, set a first pump configuration and then the final one when the butterfly valve is opened.
5. Do not forget to verify the oil levels and the proper operation of the water pumps during the whole run.
6. Once the selected pumping configuration is started, adjust the stagnation pressure with the gas inlet and the static pressure in the test chamber with the butterfly valve.

6. Image of the Baseline

1. Do this step before undertaking the experiments. The baseline corresponds to the flat plate in the rarefied flow without firing the discharge. From this, one can calculate the baseline shock wave angle, which is the angle naturally formed between the shock wave and the flat plate because of the supersonic speed of the flow.
2. Use the luminescent technique to visualize the airflow and the shock wave (see **Figure 9**).
3. **The luminescent technique**
    1. Install a plate, made from copper or any other conductive material, of dimensions 20 cm x 40 cm above the exit of the nozzle and connect it to the DC power supply.
    2. Install another copper plate of the same dimensions under the exit of the nozzle. This one is grounded. The copper plates must not interfere with the flow.
    3. When the facility is running and delivers the scheduled flow, supply the connected copper plate with -100 V. This will lead to a weak ionization of the flow and allows the visualization of the shock wave but will not influence it.
    4. Utilize each of the diagnostic tools to get baseline results that will serve as comparators for the test results.

7. Firing the Discharge

1. Switch on the high-voltage power supply and gradually increase the voltage until the emergence of the glow discharge above the active electrode. Take note of this voltage, which is the breakdown voltage. Here, the breakdown voltage was -0.40 kV.
2. Decrease the voltage by -250 V steps and take a set of 250 iCCD images at each voltage. Adjust the exposure time and the gain to get the highest contrast picture but make sure to not saturate the image.
3. Take note of the current delivered when biasing the active electrode with the high voltage.
4. Simultaneously acquire the temperature distributions on the surface with the IR camera.
5. Carry out Pitot profiles for different positions of the Pitot probe for different voltages under the same conditions to get a trend. A standard procedure to establish a complete mapping of the pressure is given below.
    1. Establish a vertical profile at X=0 cm, Y=0 cm, Z=0 cm by increasing the Z-position of the Pitot probe. Register the pressure value after stabilization for each mm in the boundary layer, each 5 mm in the shock wave, and each cm when exiting the flow core.
    2. Move the Pitot probe to X=17.5 cm, which corresponds to the middle of the active electrode and repeat step 7.5.1.
    3. Move the Pitot probe to X=50 cm, which corresponds to the middle of the flat plate, and repeat step 7.5.1.
    4. Move the Pitot probe to X=0 cm and Z=20 cm to perform a longitudinal profile (in the X-position, the length of the model) and move the Pitot probe by 5 mm.
    5. Repeat step 7.5.4 at position X=0 cm and Z=40 cm.

8. Post-Treating the Results

1. **iCCD imaging**
    1. Process the iCCD set of images with software such as Matlab or ImageJ. For all the discharge conditions, add the 250 images to increase the intensity.
    2. Improve the contrast and make the shock wave angle as visible as possible.
    3. Measure the shock wave angles for each discharge voltage and draw the trend line.
    4. Take measurements of the shock wave stand-off distance from the leading edge.

2. **Infra-red tomography**
    1. Plot the temperature distributions along the black lines for each discharge voltage.
    2. Find the maximum surface temperature and plot it versus the discharge voltage.

3. **Pitot pressure measurements**
    1. As the experimental conditions correspond to the rarefied regime, do any necessary orifice corrections according to the flow conditions and the Pitot reference dimensions as specified by Potter *et al.*[17,18,19].
    2. Draw all the Pitot profiles on the same graph to aid in further comparison.
    NOTE: It can be useful to simulate the experimental case with a numerical code (in this paper, a Monte-Carlo probabilistic code is used) to calibrate the experimental Pitot profiles.

Representative Results

The experiments are carried out in the wind tunnel MARHy at the ICARE laboratory located in Orléans (CNRS, National Scientific Research Center, France). MARHy is a low-density facility used for both academic and industrial research. The wind tunnel was built in 1963 at the "Laboratoire d'Aérothermique" and was known as the "SR3" wind tunnel[20] until its relocation in 2000 at the CNRS Orléans. The MARHy wind tunnel can be equipped with a wide range of nozzles allowing the generation of subsonic, supersonic, and hypersonic flows from Mach 0.8 to Mach 21, and covers a large range of Reynolds numbers from 10^2 up to 10^5 for a reference length of 100 mm (corresponding to the length of the flat plate used as a model). These flow conditions reconstitute most of the reentry vehicles' flight corridors from 140 km to 67 km of altitude, making this facility unique in Europe. **Figure 10** exhibits the facility which can be divided in three parts: the settling chamber with a diameter of 1.3 m and a length of 2.0 m, the test chamber with a diameter of 2.3 m and a length of 5.0 m, and a third chamber in which a diffuser is installed and connects the pumping group to the facility through a vacuum gate. The pumping group is composed of 2 primary pumps, 2 intermediary Roots blowers, and 12 Roots blowers. Its performance makes it able to ensure low-density flow conditions continuously.

In this study, the entry conditions are simulated by a flow at Mach 4 and a static pressure of 8 Pa corresponding to a geometric altitude of 72 km. **Table 1** compiles the overall operating conditions for each nozzle, where P represents the pressure, T the temperature, ρ the volumetric mass density, U the flow velocity, M the Mach number,λ the mean free path, and Re the Reynolds number based on the flat plate length L = 100 mm and calculated with the relation $Re = U_1 L/v_1$, where v is the kinematic viscosity in m^2/s because $v = \mu/\rho$. The air flow distribution is uniform through the test sections with a core diameter of 8 cm and a core length of 20 cm. Previous work had been undertaken with a flow at Mach 2 and a static pressure of 8 Pa corresponding to a geometric altitude of 67 km[21].

The model under investigation is a flat plate (50 mm-long, 80 mm-wide and 4 mm-thick) with a sharp leading edge (15°), as shown on **Figure 1**. The plasma actuator induces very high wall temperatures and thus, models must be manufactured in a heat-resistant material. The flat plates are made of quartz and the position of the model in the test chamber is sketched on **Figure 5**. The two electrodes setting the plasma actuator are manufactured in aluminum and designed with the following dimensions: 50 mm-width, 35 mm-length, and 80 µm-thickness. These electrodes are flush mounted on the upper surface of the flat plate. Depending on the nozzle, the core of the generated flow will have specific dimensions and the models must be adapted to these cores. Therefore, the width of the model strongly depends on the studied flow. However, to maintain a certain level of coherence, the ratio of the active electrode on the surface of the model is kept at 35%. The electrode located closest to the leading edge is defined as the cathode, or active electrode, and is connected to a high voltage DC power supply through a current limiting resistor (R_s = 10.6 kΩ) while the second electrode is grounded. The DC power supply is voltage-regulated and delivers the discharge current I_{HV} corresponding to the chosen V_s voltage. The voltage applied to the active electrode, V_{HV}, is then calculated with the following relation: $V_{HV} = V_s - R_s I_{HV}$. V_s and I_{HV} are read directly on the power supply. This procedure ensures the stability of the discharge conditions.

The adequate operation of the supersonic wind tunnel MARHy is based on accurate measurements of the stagnation and test section pressures. Capacitive sensors are used to measure the stagnation pressure, P_0, and the static pressure, P_1, and the pressure above the flat plate when combined to a Pitot probe. The Pitot tube is a flat-ended tube made of glass to avoid electrical interactions with the discharge. Its dimensions are D = 6 mm for the external diameter and d = 4 mm for the internal one (see **Figure 7** that shows the Pitot tube above the flat plate at position X = 50 mm, Y = 0 mm, Z = 0 mm which corresponds to the middle of the flat plate). The pressure mapping above the plate is ensured with a 3-axis traversing system, controlled by a computer. The step resolution of the Pitot probe on each axis is 0.1 mm ± 0.02 mm for each position.

A MKS control unit with a 12-bit resolution is linked to the manometers associated to P_0 and P_1, whereas a MKS control unit is used for the Pitot probe acquisition. The 10 V output of each MKS control unit is read by an acquisition card storing the pressures values during experiments. **Figure 8** exhibits the manometers' positions.

An iCCD camera (1024 x 1024-pixel array) equipped with a VUV (Visible-Ultraviolet) objective lens (94 mm, f =4.1) is used for the flow visualization. As shown in **Figure 8**, the iCCD camera is placed perpendicular to the flow axis and collects light through a fluorine window located in the wall of the test section chamber.

An infrared camera is placed on the top of the wind tunnel focusing on the model through a zinc selenide (ZnSe) window compatible with the IR wavelength range of the camera, as drawn on **Figure 8**. This device follows and records the live evolution of the surface temperature of the model. The IR camera is equipped with a QWIP-type (Quantum Well Infrared Photodetector) IR photo-detector composed of a 320 x 240 pixel array.

First, the baseline is defined. It corresponds to the flow behavior around the model without any actuation. The flow conditions are detailed in **Table 1**. **Figure 9** presents the images of the baseline recorded with the iCCD camera and visualized using the luminescent discharge technique. The software ImageJ was used to improve the image contrast and thus, allowed a more precise determination of the shock wave. For this flow at Mach 4 for a static pressure of 8 Pa, the shock is sharp and attached to the leading edge of the flat plate. Therefore, the shock wave shape is fitted by a linear equation and a shock wave angle of β = 23.2°± 0.5 is detected.

The experimental and numerically normalized Pitot profiles are displayed on the same plot in **Figure 11** to calibrate the experimental profiles and confirm their validity. The normalization is made with the value of the maximum Pitot pressure of each profile. The profiles are plotted for the abscissa X = 50 mm (in the middle of the flat plate). Indeed, the Pitot pressure gradients are higher as distance increases from the leading edge as the gas compression due to the shock wave has a triangle shape. Therefore, it is easier to compare the profiles if the gradients are large enough. The knee visible on the profiles represents the shock transition where the shock wave and the boundary layer are merged.

As was observed, the experimental profiles were in good agreement with those calculated with the code. The shock wave angle was estimated with the position of the knee region, which gave an experimental shock angle of β = 23.5° ± 0.7°, which was very similar to the value found with the iCCD images.

The discharge was created by applying a negative DC potential to the active electrode. **Figure 12** shows the current-voltage (I_{HV}-V_{HV}) characteristics of the plasma actuator. The discharge ignited at the voltage V_{HV} = -0.40 kV. The discharge current increased with the applied voltage, corresponding to the abnormal glow discharge regime. **Figure 13** shows a picture of the discharge. The plasma has the shape of a flame and goes straight upward. It is assumed that as the static pressure is low, the plasma is very diffuse and is created between the cathode and the top of the experimental chamber instead of the grounded electrode. The plasma can easily be divided in two parts, a bright one, the negative glow, and a dark one, known as the cathodic or plasma sheath. When increasing the discharge power, the shock wave is pushed away and thus, the shock wave angle increases as shown in **Figure 14** where the shock waves are presented for two different discharge powers. **Figure 15** shows the variation of the shock wave angle with the discharge current. One can observe that the higher the discharge current, the higher the increase in the shock wave angle. Knowing that the shock wave angle is inversely proportional to the Mach number, it can be deduced from this result that the Mach number of the flow over the model decreases when switching on the discharge and gets even lower when increasing the discharge power.

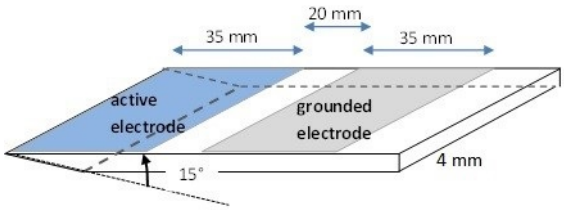

Figure 1: Scheme of the plasma actuator mounted on the flat plate.
Figure 1 shows a scheme of the positions on the model and sizes of the electrodes constituting the plasma actuator.

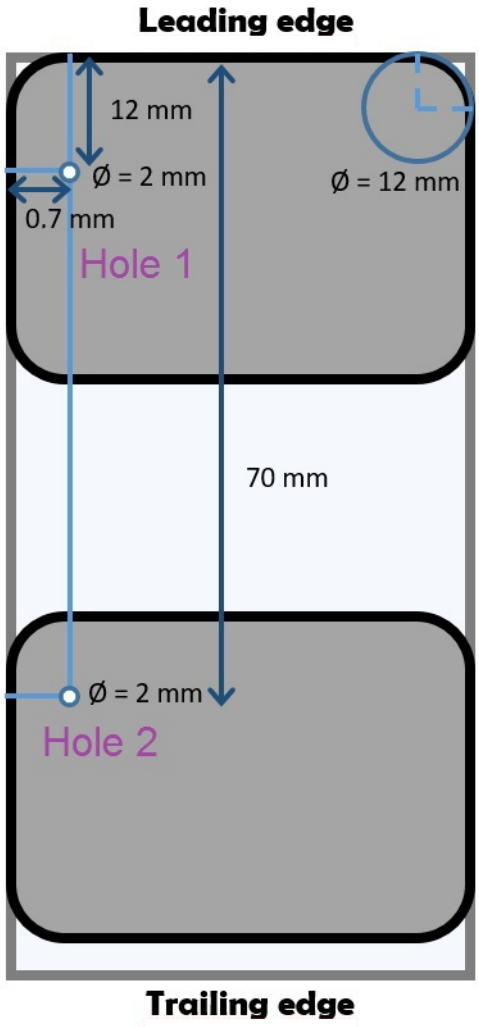

Figure 2: Top view of the flat plate with the hole positions.
Figure 2 gives the positions and dimensions of the holes for the cable connections and the curvature radius of the electrodes.

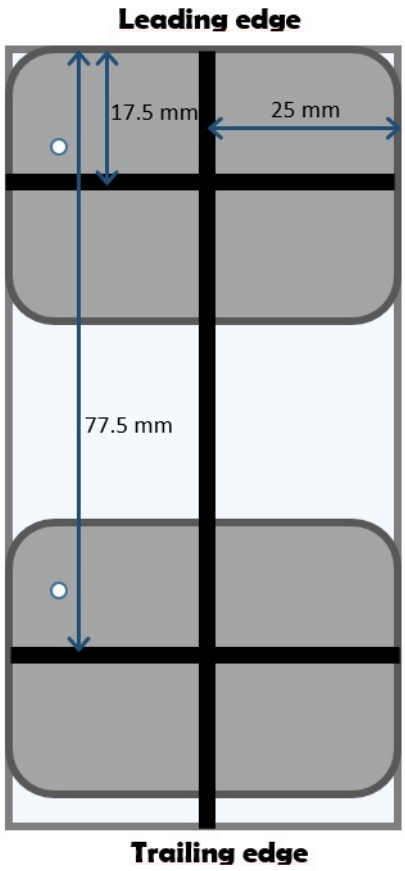

Figure 3: Top view of the flat plate with the black painted lines for the IR camera.
Figure 3 shows an overview of the positions of the black painted lines drawn on the flat plate to allow better temperature detection with the IR camera.

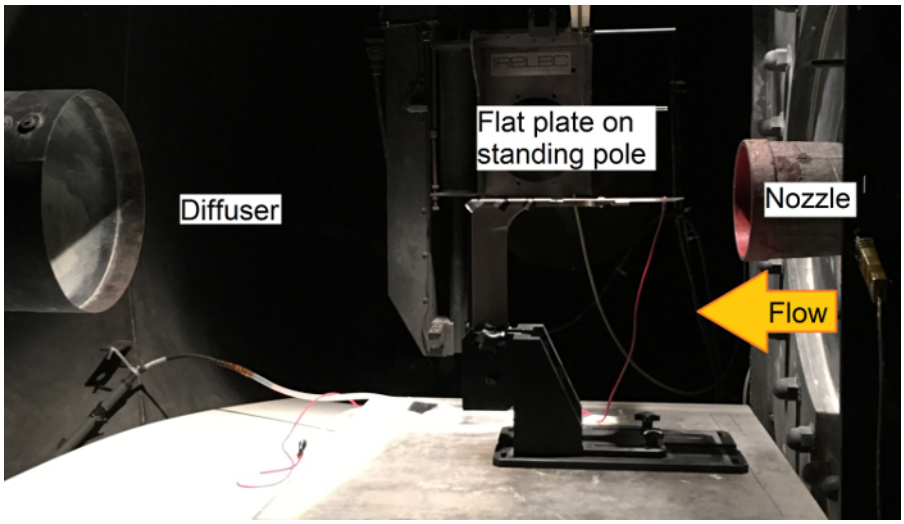

Figure 4: Photo of the experimental setup in the test chamber.
Figure 4 illustrates the different elements in the test chamber with a picture. The nozzle, the flat plate on the standing pole, and the diffuser can be distinguished. Please click here to view a larger version of this figure.

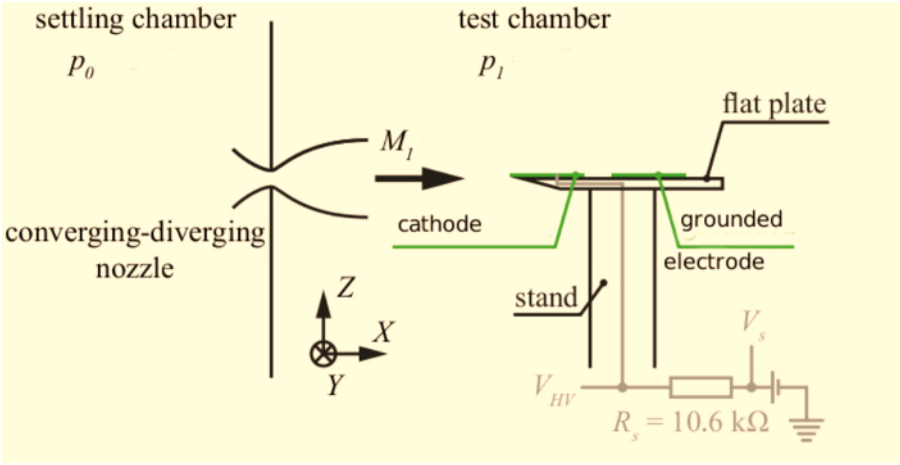

Figure 5: Experimental set-up.
Figure 5 is a schematic of the whole experimental setup with the direction of the axis, the position of the power supply connections, and the flow direction. Please click here to view a larger version of this figure.

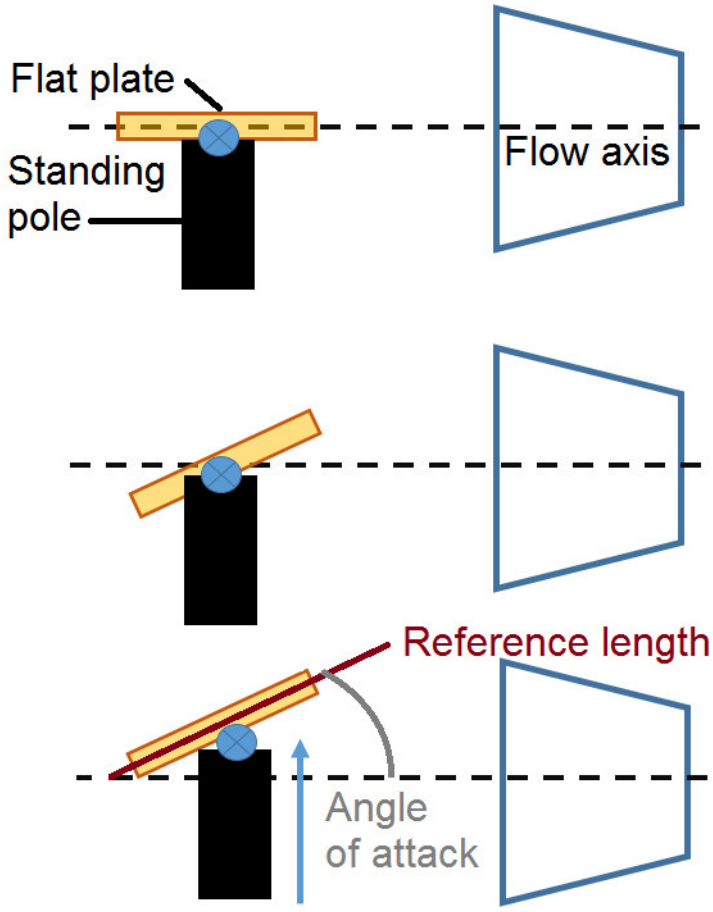

Figure 6: Scheme of setting up the angle of attack.
Figure 6 helps in understanding how to set up an angle of attack for the model with the standing pole. Please click here to view a larger version of this figure.

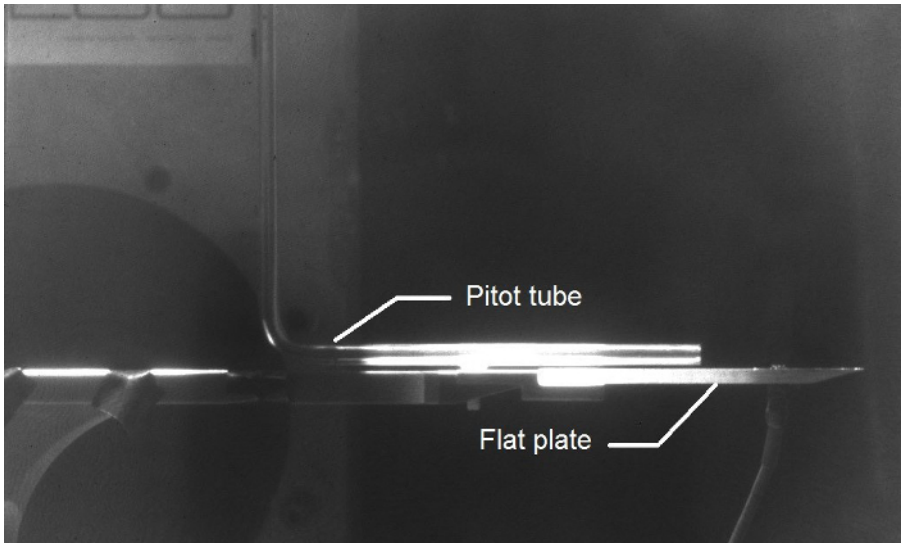

Figure 7: iCCD image of the Pitot tube located in the middle of the flat plate (X=50 mm, Y=0 mm, Z=0 mm).
Figure 7 is a picture of the Pitot tube above the flat plate and allows the understanding of the Pitot design. Please click here to view a larger version of this figure.

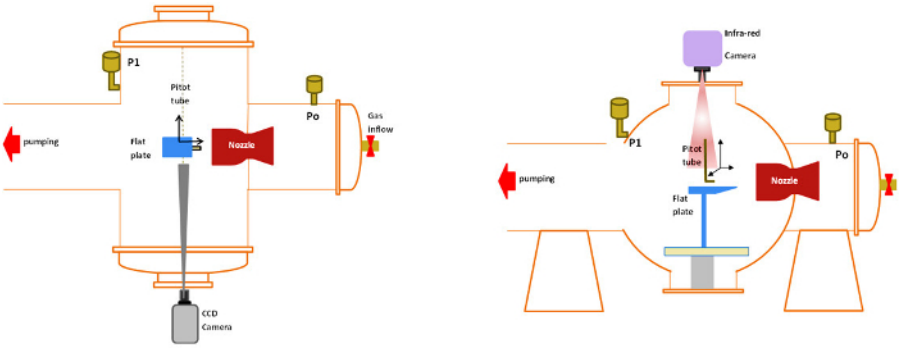

Figure 8: Schematic view of the wind tunnel and configuration of the diagnostics.
Figure 8 shows the positions of the different diagnostics such as the iCCD camera, the manometers, and the IR camera. Please click here to view a larger version of this figure.

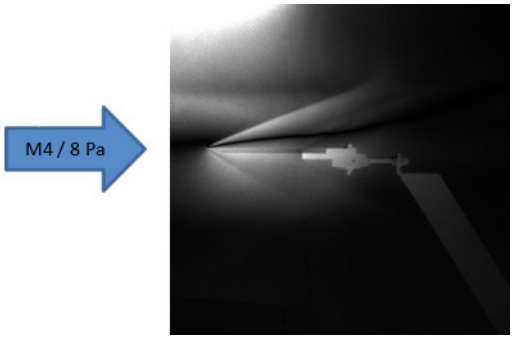

Figure 9: Experimental baseline flow field obtained with the iCCD images.
Figure 9 is an improved iCCD image of the baseline obtained with the luminescent technique. It demonstrates the shock wave obtained for the flat plate in a Mach 4 flow at a static pressure of 8 Pa.

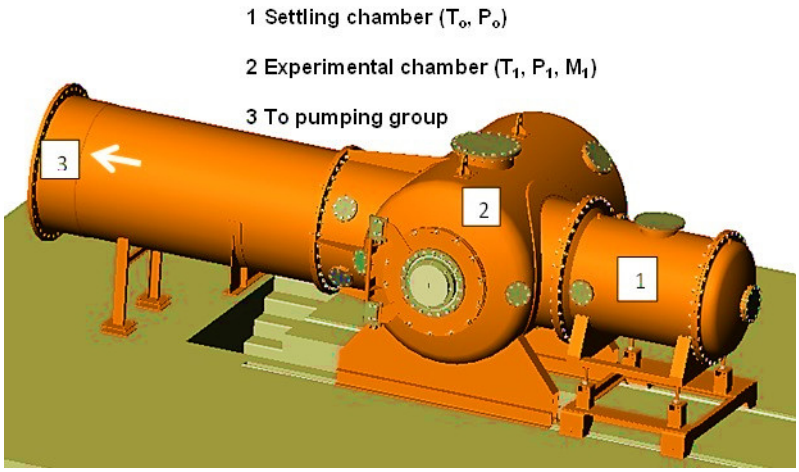

Figure 10: The MARHy wind tunnel layout.
Figure 10 is a 3D layout of the MARHy wind tunnel which details the three main parts: the settling chamber, the test chamber, and the diffuser. It gives the parameters linked to each of these parts.

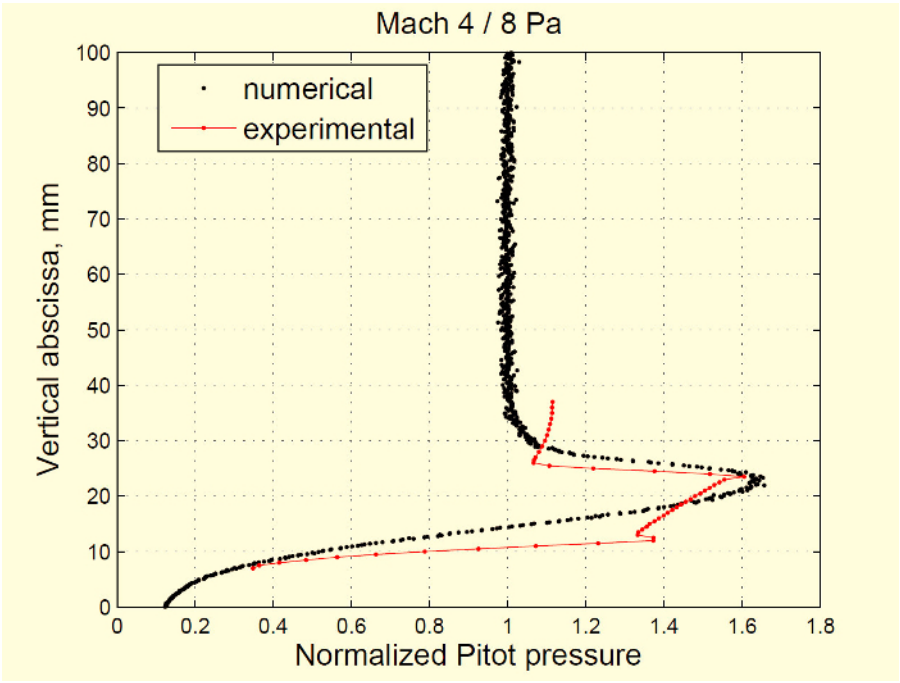

Figure 11: Numerical and experimental Pitot probes profiles at X = 50 mm for the baseline case.
Figure 11 is a plot exhibiting the numerical and experimental Pitot probe profiles at X = 50 mm for the baseline case. This figure is used to validate the experimental profile and confirm the determined shock wave angle. Please click here to view a larger version of this figure.

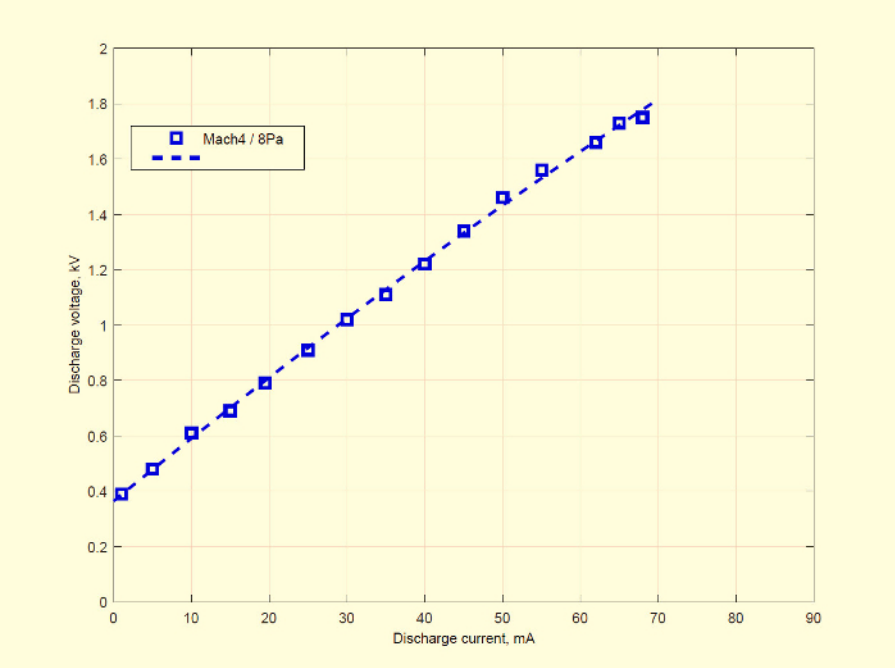

Figure 12: Current-voltage characteristics of the plasma actuator.
Figure 12 illustrates the discharge current corresponding to the applied discharge voltage. This figure aids in understanding the performance of the plasma actuator and its energy consumption. Please click here to view a larger version of this figure.

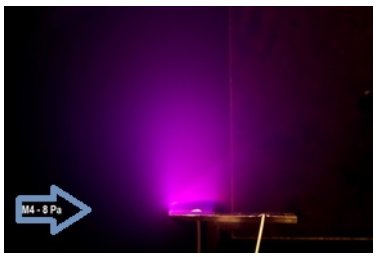

Figure 13: Picture of the flat plate with discharge fired.
Figure 13 is a picture of the plasma created above the flat plate when the plasma actuator is on and the flat plate is placed in the Mach flow at a static pressure of 8 Pa.

Figure 14: Picture of the flat plate with the discharge fired for two different discharge currents.
Figure 14 exhibits the shock wave modifications obtained for two different discharge currents on the same picture to illustrate the effect of the plasma actuator on the shock wave angle when increasing the discharge current.

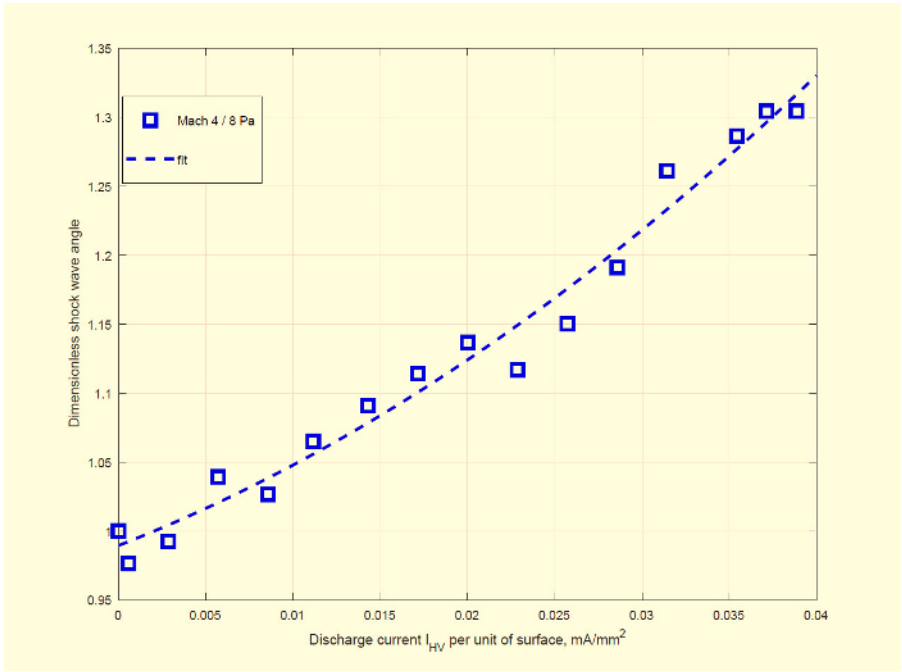

Figure 15: Dimensionless shock wave angles versus the discharge current per unit of surface.
Figure 15 is a plot of the dimensionless shock wave angles versus the discharge current per unit of surface. It shows the increase of the shock wave angle with the discharge current. Please click here to view a larger version of this figure.

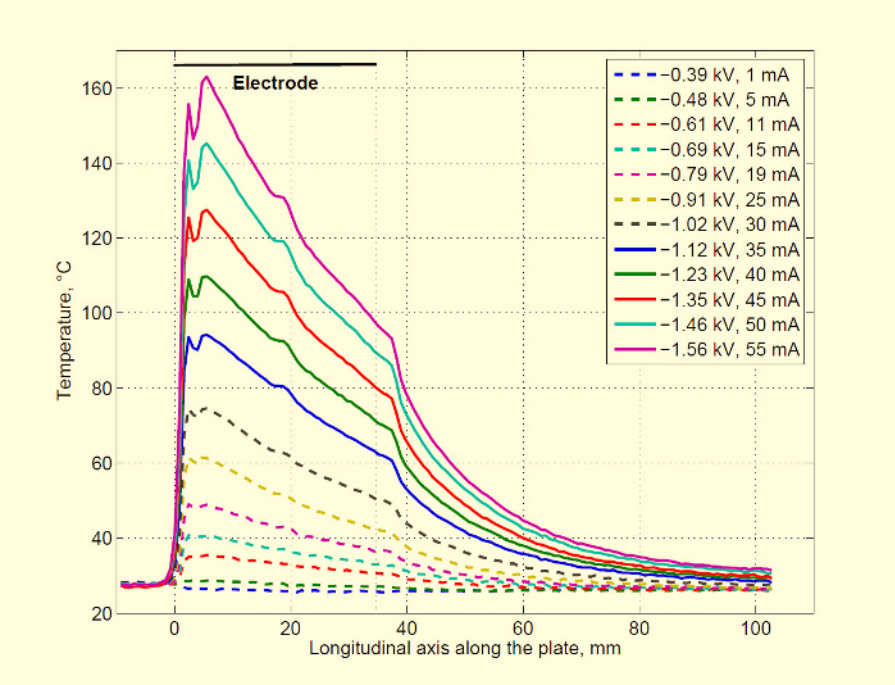

Figure 16: Temperature profiles along the X-axis of the flat plate.
Figure 16 illustrates the evolution of the temperatures along the X-axis of the flat plate for different power discharge settings. It shows the particular shape of the temperature profiles and the temperature values demonstrating that the surface heating is negligible. Please click here to view a larger version of this figure.

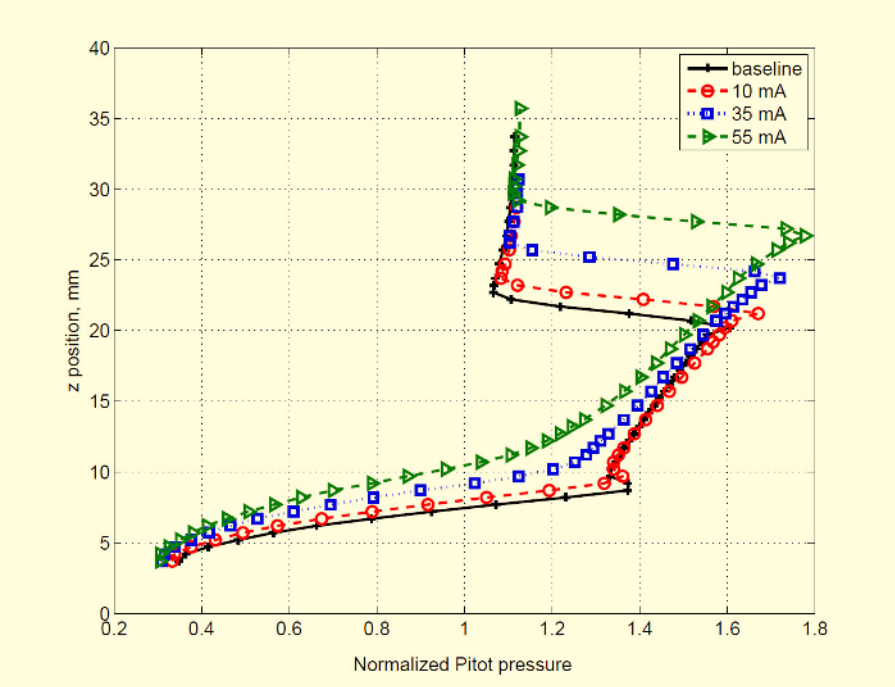

Figure 17: Effect of the plasma discharge on the Pitot probe profiles measured at X = 50 mm.
Figure 17 illustrates the Pitot pressure profiles above the middle of the flat plate for different discharge currents. This plot demonstrates the increase in the knee height, confirming the shock wave angle increase. Furthermore, it shows the low increase of the boundary layer and thus, its low impact on the shock wave angle increase. Please click here to view a larger version of this figure.

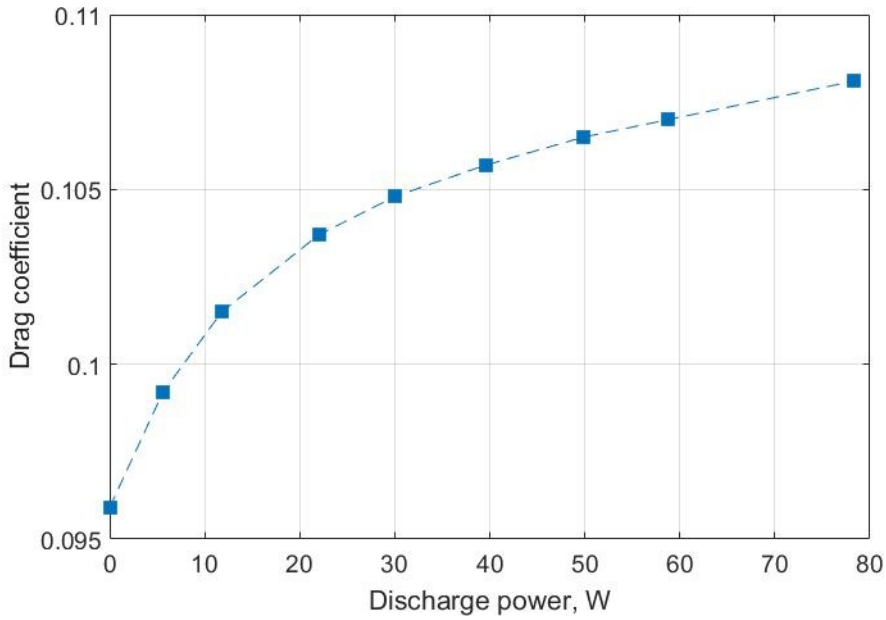

Figure 18: Estimation of the drag induced by the plasma actuator over the flat plate.
Figure 18 plots the drag coefficient versus the discharge power and demonstrates that it increases with the discharge power. This is related to the increase in the shock wave angle which also increases with the discharge power.

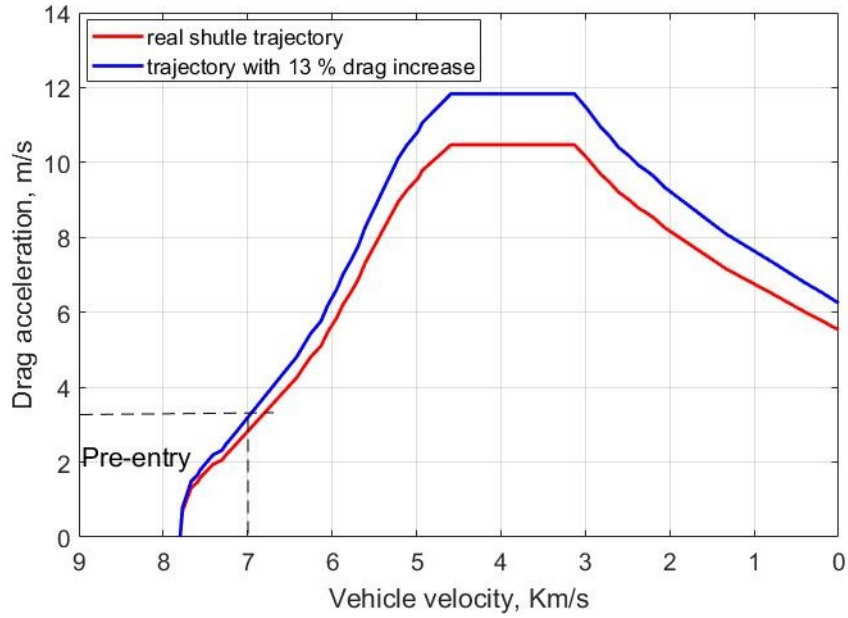

Figure 19: Effect of the plasma actuator on the entry guidance drag velocity profile.
Figure 19 demonstrates the effect of the plasma actuator overall on the entry guidance of a reentry vehicle. Indeed, in the first phase of the reentry for a given velocity, if the drag is increased +13% with the plasma actuator, it would give a lower effective velocity.

Stagnation conditions	Free stream conditions
P_0 = 1214 Pa	P_1 = 8 Pa
T_0 = 293 K	T_1 = 70 K
ρ_0 = 1.44x10^{-2} kg.m^{-3}	ρ_1 = 3.99x10-4 kg.m^{-3}
	μ_1 = 1.10x10^{-5} Pa.s
	U_1 = 670 m.s^{-1}
	M_1 = 4
	λ_1 = 0.067mm

Table 1: Operating conditions.
Table 1 shows the main parameters of the flow studied in this paper as the Mach number, the Reynolds number, or the static pressure.

Discussion

The described experimental protocol presents some critical steps. The first point concerns the repeatability of experiments because, for a given experimental condition, several experimental campaigns are needed. Indeed, to have a complete physical analysis, different diagnostics are used that cannot be applied simultaneously. This implies that the experimental set-up (model, electrode size and shape, position of the model in the test chamber, *etc.*) must be rigorously the same throughout the experiments. Even slight differences can induce different discharge conditions modifying the plasma actuator effects and prevent the results from being directly comparable. The other point directly impacts the shock wave angle measurements. Indeed, each iCCD image needs specific post-processing, and is analyzed manually. Therefore, it is essential to apply a well-run method for every post-processing. Furthermore, the shock wave angles are also determined from Pitot probe profiles and compared to angles detected with the iCCD images to strengthen the measurements.

The technique of utilizing plasma actuators also presents some issues. The main limitation of such actuators is due to the flow conditions, especially the pressure and, thus, the altitude of the atmospheric re-entry of the spacecraft. Plasma actuators have to be characterized in different flow regimes in terms of speed and pressure to extrapolate their behavior to real cases. For this purpose, it is necessary to deeply understand the plasma physics and its coupling with the flow to overcome these challenges. Some authors incriminated thermal effects (bulk and surface) for the shock wave modifications in supersonic conditions[22]. Shin *et al.* investigated thermal effects with two distinct discharge modes, where an increase in gas temperature was observed; nevertheless, no clear evidence of plasma effects on the flow was identified[15].

The present paper shows that other physical aspects related to the discharge, rather than thermal considerations, have to be taken into account to explain the flow modifications. **Figure 16** displays the temperature distributions along the longitudinal axis of the model. The plots show that the plasma actuator heats the surface of the model, although the distribution is non-uniform and the maximum values are found close to the leading edge. The non-uniformity is induced by variation in the electric field along the X-direction and this electric field is highest close to the leading edge of the flat plate[23]. For a given value of the discharge current I_{HV}, the plasma discharge without the Mach 4 flow (static pressure set to 8 Pa) induced a similar heating of the flat plate, with a temperature distribution similar (both in value and shape) to the temperature distribution when the Mach 4 flow is operating. This result confirms that the heating of the flat plate surface is mainly related to a discharge effect and not influenced by the interaction between the Mach 4 air flow and the flat plate surface. Moreover, the surface heating induces a displacement effect: the flow viscosity above the heater is modified, inducing an increase in the laminar boundary layer thickness, and consequently, the shock wave is shifted outward from the flat plate surface (*i.e.*, the shock wave angle increases). This effect can be observed more clearly on **Figure 17** where four Pitot pressure profiles are presented: one corresponds to the baseline, and the others correspond to the cases when different discharge powers are supplied. On the shape of the profiles measured at X = 50 mm, the knee geometry is found at a higher position on the Z-axis, meaning that the thickness of the boundary layer has increased and therefore, the shock wave angle increased as well.

Experiments carried out with a Mach 2 flow and a static pressure of 8 Pa showed that the thermal effects accounted for only 50% of the shock wave angle increase and the remaining 50% of changes were due to ionization effects[21]. For Mach 2 and Mach 4 flows, the surface temperature distributions are similar, although the temperature gradients are higher with the Mach 2 flow. Therefore, one can assume that the ionization effect would be even greater with the Mach 4 flow than the 50% estimated in previous studies[21], meaning that the influence of surface heating on the shock wave modification will be even less important.

During atmospheric re-entries, atmospheric drag is used to slow down the vehicle, but the amount of energy to dissipate in these conditions is enormous. The rate of energy dissipation is then estimated to be proportional to the cube of the vehicle speed, inducing very high temperatures on the spacecraft which may produce serious damage if thermal protections are not sufficient. Optimal return trajectories are designed to obtain the minimum return cost defined as the sum of the mass propellant consumed by the space vehicle to de-orbit and the mass of thermal protections. However, reduction of thermal protection could be a way to decrease the cost of future missions. For this purpose, one idea is to increase the drag force with the aim of decelerating the vehicle, and the use of plasma actuators is a potential method to achieve this goal.

In order to estimate the efficiency of plasma actuators in heat load reduction, numerical simulations corresponding to the presented experimental conditions have been carried out to determine the aerodynamic drag forces induced by the discharge over a flat plate at Mach 2 and 8 Pa[2]. The surface heating produced by the plasma discharge is numerically simulated reproducing the shock wave angle modifications observed experimentally. Results showed that, with only the surface heating, the shock wave angles are half those determined with the plasma actuator. The drag force was then calculated from the surface pressure gradient obtained for each experimental condition. An empirical law was obtained, linking the shock wave angle and the drag coefficient based on the effect of the surface heating. An extrapolation of this law allowed the determination of the drag coefficients corresponding to the shock waves angles obtained with the plasma actuator. **Figure 18** presents the

behavior of the drag coefficient with the discharge power applied to the plasma actuator. An increase of 13%for the drag coefficient is expected in our experimental conditions when applying 78.3 W to the plasma actuator. For the re-entry of a space shuttle in the mold of Columbia, a rough estimation of the drag increase impact can be obtained from the entry guidance drag velocity profile[24]. **Figure 19** presents the space shuttle re-entry guidance in terms of drag acceleration, as a function of the relative velocity, for the real trajectory and for the trajectory with an increase of 13% for the drag coefficient. The shift of the new trajectory shows that the shuttle velocity decreases about 7% for velocities around 7 km/s corresponding to the beginning of the atmospheric entry. As the heat flow is proportional to the power 3.15 of the shuttle speed, the speed has a drastic influence on the heat flow, leading to a decrease of 26% of the heat flow through 1 m^2/s of the Space Shuttle surface at the stagnation point[25]. Taking into account that the mass of the heat protection in the shuttle is of 9,575 kg and that the decrease in the heat flow is proportional to the mass protection[25], 2.5 tons of the shuttle mass could be saved with a plasma actuator. In future applications, the plasma actuators could even be extended to control a full trajectory.

Disclosures

The authors have nothing to disclose.

Acknowledgements

The authors acknowledge the French Government's Investissement d'Avenir program: Laboratoire d'Excellence CAPRYSSES (grant no. ANR-11-LABX-0006-01). Additional funding is provided by the Région Centre with the PASS grant (convention no. 00078782).

The authors would furthermore like to acknowledge the constructive feedback from the reviewers.

References

1. Sellers, J. J., Astore, W. J., Giffen, R. B., Larson, W. J. *Understanding space: An introduction to astronautics. Primis.* (2000).
2. Coumar, S., Joussot, R., Parisse, J.-D., Lago, V. Influence of a plasma actuator on aerodynamic forces over a flat plate interacting with a rarefied Mach 2 flow. *IJNMHFF.* **26** (7), 2081 - 2100 (2016).
3. Joussot, R., Coumar, S., Lago, V. Plasmas for High Speed Flow Control. *Aerospace Lab.* **10,** (2015).
4. Kimmel, R. L., Hayes, J. R., Menart, J. A., Shang, J. Effect of surface plasma discharges on boundary layers at mach 5. *AIAA Paper.* **0509** (2004).
5. Kuo, S. P., Bivolaru, D. The similarity of shock waves generated by a cone-shaped plasma and by a solid cone in a supersonic airflow. *Phys. Plasmas.* **14** (2), 023503-023508 (2007).
6. Kuo, S. P. Plasma mitigation of shock wave: experiments and theory. *Shock Waves.* **17** (4), 225-264 (2007).
7. Leonov, S. B., Yarantsev, D. A., Gromov, V. G., Kuriachy, A.P. Mechanisms of flow control by near-surface electrical discharge generation. *AIAA Paper.* **780** (2005).
8. Leonov, S. B., Yarantsev, D. A. Near-surface electrical discharge in supersonic airflow: Properties and flow control. *J. Propul. Power.* **24** (6), 1168-1181 (2008).
9. Leonov, S. B. Review of plasma-based methods for high-speed flow control. *AIP Conf. Proc.* **1376**, 498-502 (2011).
10. Starikovskiy, A., Aleksandrov, N. Nonequilibrium Plasma Aerodynamics. *Aeronautics and Astronautics INTECH Open Access Publisher.* (2011).
11. Cahn, M. S., Andrew, G. M. Electrodynamics in supersonic flow. *AIAA 6th Aerospace Sciences Meeting.* (New York) (1968).
12. Roth, J. R. Physics and phenomenology of plasma actuators for control of aeronautical flows. *J. of Phys. D.* **40** (3) (2007).
13. Bletzinger, P., Ganguly, B. N., Van Wie, D., Garscadden, A. Plasmas in high-speed aerodynamics. *J. of Phys. D.* **39**, 33-57 (2005).
14. Fomin, V. M., Tretyakov, P. K., Taran, J. P. Flow control using various plasma and aerodynamic approaches. *Aerospace Sci. and Tech.*, **8**, 411-421 (2004).
15. Shin, J., Narayanaswamy, V., Raja, L. L., Clemens, N. T. Characteristics of a plasma actuator in Mach 3 flow. *In 45th AIAA Aerospace Sciences Meeting and Exhibit.* (Reno) (2007).
16. Poggie, J., Adamovich, I., Bisek, N., Nishihara, M. Numerical simulation of nanosecond-pulse electrical discharges. *PSST.* **22** (1), 015001 (2012).
17. Schaaf, S.A. The Pitot probe in low-density flow. *AGARD.*, **525** (1966).
18. Potter, J., Kinslow, M., Boylan, D. An influence of the orifice on measured pressures in rarefied flow. *Rarefied Gas Dynamics,* **2**., 175 (1965).
19. Potter, J. Techniques Expérimentales Liées à l'Aérodynamique à Basse Densité. *AGARD.*, **318** (1990).
20. Allègre, J. The SR3 low density wind tunnel-Facility capabilities and research development. *28th Joint Propulsion Conference and Exhibit.* **3972** (1992).
21. Joussot, R., Lago, V., Parisse, J.-D. Quantification of the effect of surface heating on shock wave modification by a plasma actuator in a low-density supersonic flow over a flat plate. *Experiments in Fluids.*, **56** (5), 102 (2015).
22. Semenov, V. E., Bondarenko, V. G., Gildenburg, V. B., Gubchenko, V. M., & Smirnov, A. I. Weakly ionized plasmas in aerospace applications. *Plasma physics and controlled fusion.*, **44**(12B), B293 (2002).
23. Parisse, J.-D., Léger, L., Depussay, E., Lago, V., Burtschell, Y. Comparison between Mach 2 rarefied airflow modification by an electrical discharge and numerical simulation of airflow modification by surface heating. *Physics of Fluids.*, **21** (10), 106103 (2009).
24. Hale, W., Chapline, G. Wings In Orbit. *Education.*, **9**, 20 (2010).
25. Bolonkin, A. A new method of atmospheric reentry for space shuttle. *AIAA Paper.*, **2006-6985**, 6-9 (2006).

